Coupling crystal plasticity and microstructure in SLM manufactured 316L parts: model development and experimental assessment

Nikita S. Kondratev, Alexey I. Shveykin, Kirill A. Romanov
Laboratory of Multilevel Structural and Functional Materials Modeling, Perm National Research Polytechnic University, Perm 614990, Russia
kondratevns@gmail.com, http://orcid.org/0000-0002-0261-3017
alexey.shveykin@gmail.com, http://orcid.org/0000-0002-2656-0781
k.a.kriv@mail.ru, http://orcid.org/0000-0002-3599-7627

Rinetta M. Mosina
Udmurt State University, Izhevsk 426034, Russia
rmfks@udsu.ru, http://orcid.org/0000-0002-1027-2857

Igor V. Shishkovsky
Samara Branch of Lebedev Physical Institute of the Russian Academy of Sciences, Samara 443011, Russia
shiv@fian.smr.ru, http://orcid.org/0000-0002-4404-9020

Evgeny V. Kharanzhevskiy
Udmurt State University, Izhevsk 426034, Russia
eh@udsu.ru, http://orcid.org/0000-0002-1525-2169

Mikhail D. Krivilyov
Udmurt State University, Izhevsk 426034, Russia, Udmurt Federal Research Center of the Ural Branch of the Russian Academy of Sciences, Izhevsk 426067, Russia
mk@udsu.ru, http://orcid.org/0000-0002-0239-2883

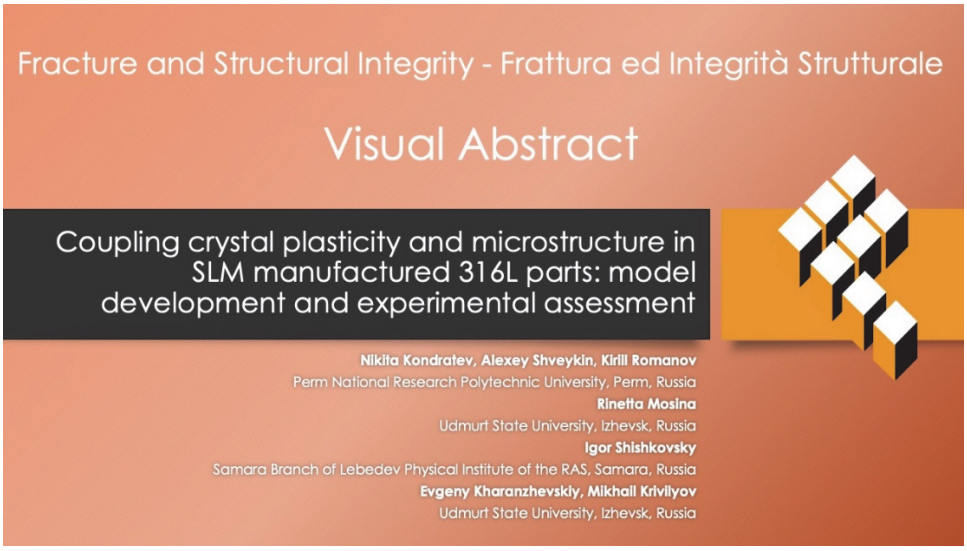

Citation: Kondratev, N., Shveykin, A., Romanov, K., Mosina, R., Shishkovsky, I., Kharanzhevskiy, E., Krivilyov, M., Coupling crystal plasticity and microstructure in SLM manufactured 316L parts: model development and experimental assessment, Fracture and Structural Integrity, 75 (2026) 373-389.

Received: 29.09.2025
Accepted: 12.11.2025
Published: 23.11.2025
Issue: 01.2026

Copyright: © 2026 This is an open access article under the terms of the CC-BY 4.0, which permits unrestricted use, distribution, and reproduction in any medium, provided the original author and source are credited.

KEYWORDS. Multi-level constitutive model, Crystal plasticity, Additive manufacturing, Selective laser melting, AISI 316L, Mechanical properties.

INTRODUCTION

Along with pressing, cutting, drilling and milling, additive 3D manufacturing is actively used to fabricate products from metals and polymers [1,2]. Additive-manufactured parts have found wide application in medicine and different industries [3,4]. This production approach uses wire or powder as feedstock materials [1,5]. With powder, selective laser melting (SLM) is used for manufacturing metallic parts [5,6]. Initially, a layer of metal powder is deposited on a metal build platform and then selectively melted by a laser. Next, the substrate plate is lowered, and the process is repeated cyclically, which finally leads to the formation of a layer-by-layer deposited product. The advantages of SLM are as follows. It allows fabrication of a wide range of complex-shaped parts without using a separate production line for each assembly component. That can drastically reduce the production time required to manufacture the products with mechanical properties comparable to traditional fabricating methods [7].

Owing to the ultra-fast heating and cooling of the material in SLM processing, the material structure got at different manufacturing regimes (laser power, scanning rate, distance between laser tracks, laser beam trajectory, powder layer thickness, chamber pressure and some others) differs substantially [8,9]. The high cooling and heating rates inherent to SLM can contribute to the occurrence of significant internal (residual) stresses and phase transformations [2]. In addition, the effective mechanical properties of a representative volume of materials are determined by their structure and deformation mechanisms realized at different scale levels [10,11]. Thus, a technologically important problem is the relationship between the structure of the SLM-fabricated samples and their mechanical properties.

A common way to get a formal description of the specified relationship is mathematical (computer) modeling. The necessity for careful examination of the material's internal structure and deformation mechanisms appeals to effective multi-level constitutive crystal plasticity models [12,13]. These models can explicitly describe the structure of materials and accommodate different scenarios that accompany inelastic deformation. Unlike macro-phenomenological models, multi-level models are more versatile and can be used for describing a wide range of thermo-mechanical effects and classes of materials [14,15].

The paper is organized as follows. Section 1 described the characteristic structure of SLM-produced samples and the mechanisms governing inelastic deformation of 316L stainless steel (SS) samples. The information was compiled after analysis of own experimental data and literature sources. Section 2 presents the governing equations of the two-level statistical constitutive model designed for the description of elastic deformations and the onset of plasticity. It also shows how the identification of model parameters is constructed. Section 3 contains the simulation results produced within the framework of the developed two-level constitutive model, including its stability evaluation. The information about the comparison between the predicted and experimental data, along with the paper outcomes, is provided.

Processing parameter	Value
Laser power	113 W
Laser beam diameter	55 μm
Hatch space	50 μm
Thickness of a single layer	20 μm
Scanning strategy	Squares X-Y, 1-4 mm
Scanning speed	750 mm/s
Flow rate (Ar)	2.5 m/s
Chamber pressure	1 bar
Oxygen content	< 0.3%

Table 1: SLM processing parameters used in the present study.

MATERIALS AND EXPERIMENTAL RESULTS

For our study, a series of experiments on the microstructure and mechanical characteristics of the SLM steel 316L SS samples is completed. Höganäs AB 316L powder with a particle size of 20-53 μm is used as a feedstock material. The samples are printed using the Trumpf TruPrint 1000 SLM machine (Germany) for the powder bed fusion process. The basic processing parameters are given in Tab. 1. A photograph illustrating the arrangement of the printed samples on the build platform is given in Fig. 1a. The samples were printed vertically as shown in Fig. 1b.

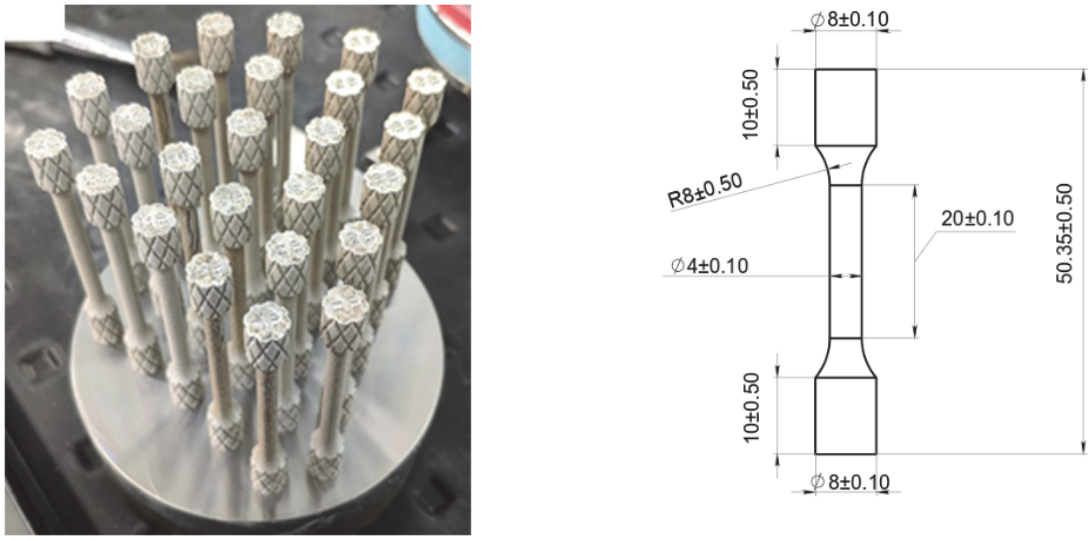

(a) (b)

Figure 1: (a) SLM 3D printed samples used for mechanical tests and microstructure assessment, (b) geometry of a round test sample.

Tensile tests of cylindrical samples are performed at a constant room temperature and at a strain rate of 10^{-3} s^{-1}. The uniaxial loading diagrams plotted for the printed vertical samples are shown in Fig. 2. The deformation domain, which corresponds to elastic tension and to the early stage of plastic deformation, is analyzed in detail in Fig. 6.

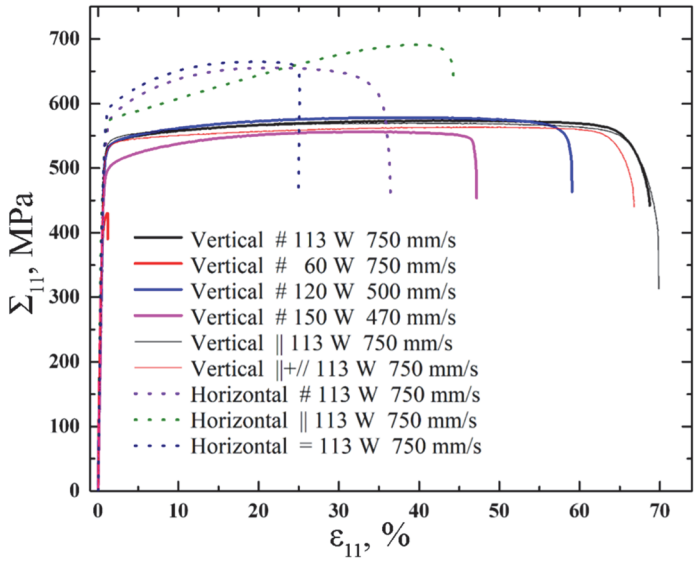

Figure 2: Experimental stress-strain curves after uniaxial loading of the vertically and horizontally SLM-printed 316L samples.

The X-ray diffraction study performed using DRON-3 and DRON-4 setups with Fe-Ka and Co-Fe radiation shows that the phase composition consists predominantly of γ-austenite (face-centered cubic lattice) and a small amount of δ-ferrite (body-centered cubic lattice). These data are consistent with the literature [16].

Two types of grain structure are frequently observed, including the planar and dendritic morphology. The microstructure type depends on such crystallization conditions as the temperature gradient, grain growth rate, undercooling degree and local chemical composition [16,17]. A higher temperature gradient promotes planar grain growth, while a lower gradient causes dendritic growth. Despite the dominance of a dendritic structure, elongated large grains can be observed under certain conditions. Fig. 3 depicts the grain microstructure of the sample in two cross sections. A coarse columnar microstructure with large γ-Fe grains is observed in all samples. The grain growth clearly proceeds across the layer boundaries, and this leads to elongated grains that span over a few printed layers. The measured characteristic lengths of grains in the build and transverse directions are about 60 and 120 μm correspondingly.

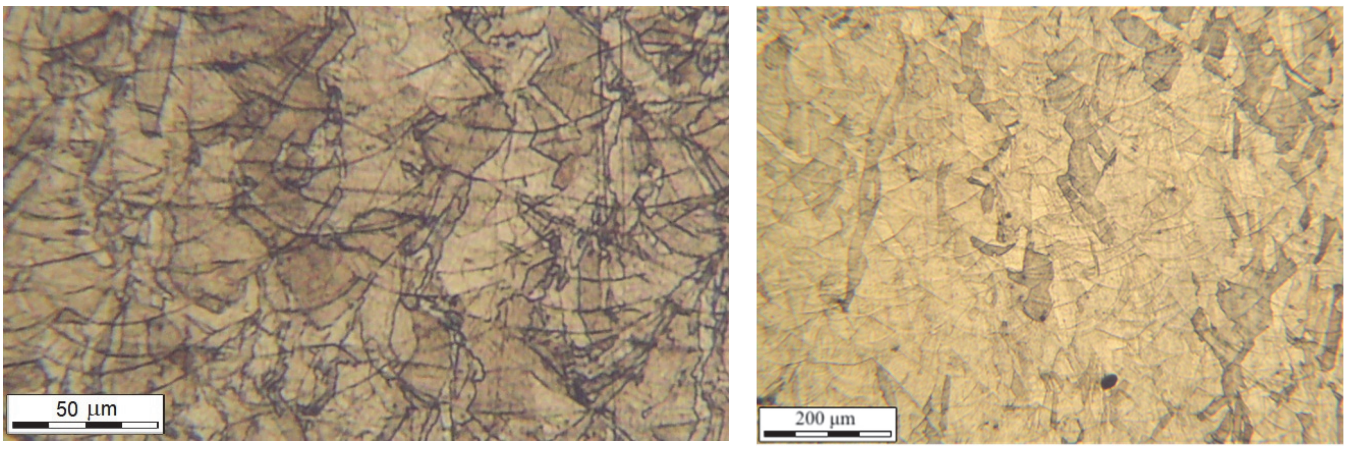

(a) (b)

Figure 3: Optical micrographs with the grain structure of the SLM-produced 316L SS samples cut vertically. The micrograph plane is transverse to the scanning direction: (a) Magnification ×300, (b) Magnification ×100.

The experimental data on the SLM 316L SS microstructure received by the authors show that austenite grains are columnar with a cellular morphology, and the characteristic values of cell lengths are tens of microns (μm). Thus, it turned out that a grain shape is close to ellipsoidal, and the largest axis is extended vertically along the build direction. Austenite grains grow in a layer-by-layer manner perpendicularly to the solid/liquid interface. Their directional solidification is determined by the heat flow through the melt layers.

The presence of non-equilibrium eutectic δ-ferrite, as well as the increased content of alloy additives Mo, Cr and Si within the cell boundaries, was reported in [16]. It was shown that the orientation of columnar grains and the crystallographic coordinate system of austenite depend on the SLM parameters (scanning modes, laser power, etc.) [16,17]. The experiments revealed the sharp crystallographic texture in the SLM 316L SS samples, which depends on the scanning strategy: (i) a dominant texture of type <100> occurs in the unidirectional scanning [17,18], (ii) a dominant texture of type <110> or a combination of textures <100> and <110> after the two-directional scanning [8,17,19].

Depending on the SLM parameters, twins (nanotwins) may develop in a lamellar form in the 316L steel. The thickness of these lamellae is of the order of several tens of nanometers [18]. The 316L SS has a low stacking fault energy, which, according to different estimates, ranges from 20 to 64 MJ/m^2 [18,20]. Therefore, the tendency of the material to undergo plane transverse slip and dislocation creep is low, and towards twinning is high. The onset of plastic deformation is predominantly triggered by the motion of edge dislocations on the {111} planes along <110> direction [20]. Sometimes, at this stage of inelastic deformation, there deformation twins occur, generated by the motion of twinning dislocations on the {111} planes along <112> direction [8,20].

According to our experimental data, laser tempering twins occur in the material microstructure after SLM processing. Such defects appear when the underlying deposited layers are lowered because of the remelting of the overlying layers. Twins in this case have a characteristic arrangement along the cell column boundaries (Fig. 4). The distance between twins is comparable to the cell size and has a value of fractions of a micron. Extensive twinning is activated during the developed plastic deformation [17,20], which has a significant impact on (i) material hardening, (ii) crystallographic texture, (iii) failure processes [20]. At high displacement gradients, owing to the increased stresses in the 316L alloy, the relaxation of elastic stresses may be caused by the phase transformation from austenite to martensite.

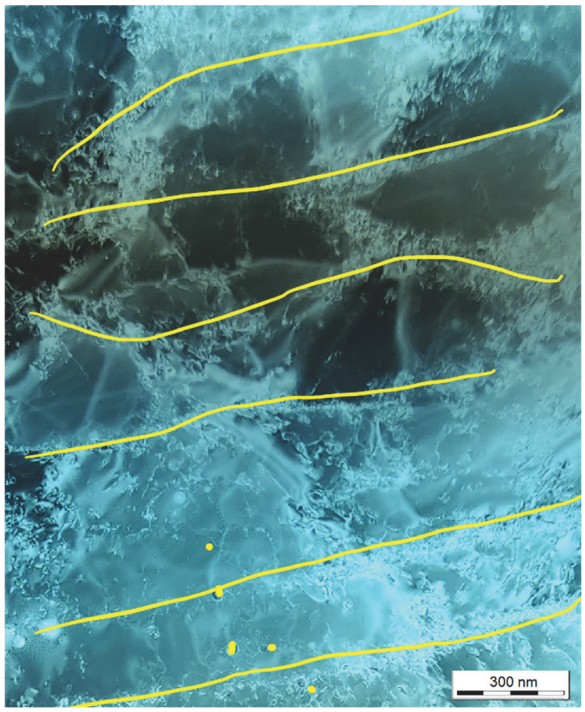

Figure 4: TEM image of the SLM-produced 316L SS sample. The yellow lines show the positions of twins relatively to the cellular structure. The distance between twin defects is between 0.1 and 0.4 μm.

Anisotropy in the mechanical properties of the SLM-fabricated 316L SS samples at the early stage of elastic-plastic deformation is primarily associated with the material texture (nonuniform distribution of grain orientations), which is generated by selective melting [8,17]. According to the preferred orientation of grains, the relaxation of elastic stresses will occur mostly because of either dislocation slip or twinning. Recent studies show that apart from the texture of materials, the anisotropy of mechanical properties depends on the construction of cells, twin boundaries, and residual stresses [17]. Some researchers reported that the mechanical behavior of the SLM-fabricated 316L SS samples is determined by the cellular structure, rather than by grain structure [21].
A constitutive model of inelastic deformation has been developed using our experimental data, which corresponds to other cited papers. This model provides an explicit description of the structure of grains and the material texture in SLM processing. Formation of twins in the original structure, the mechanisms of inelastic deformation generated by dislocation slip, and residual stresses are also accounted for. The initial critical stresses of slip are calculated using the slip length, considering perfect or partial dislocations impeded by grain boundaries, cells, or initial twins (the Hall-Petch effect). Other characteristics of the material structure are implicitly included in the model parameters during their identification on the experimental dataset. A detailed description of the model equations is provided in the next section.

TWO-LEVEL STATISTICAL CONSTITUTIVE MODEL FOR DESCRIPTION OF 316L SS DEFORMATION

In what follows, we formulate a two-level crystal plasticity model for describing the stress-strain state of inelastic deformation in SLM-manufactured AISI 316L SS samples. The models based on this approach are widely used for simulation of inelastic behavior of materials at different scale and structural levels [10] and they can be classified as of the statistical, direct and self-consistent types [15,22,23]. In direct models (CPFEM) like DAMASK [24], the finite element method is used to describe the behavior of polycrystalline material with explicit consideration of grain topology. The material model for each grain is based on crystal plasticity relations [22]. The self-consistent models account for the force load of various grains immersed in a material matrix with effective mechanical properties [23]. At last, the statistical models consider a polycrystalline representative volume composed of a set of grains. Here, effective mechanical properties at the macroscale are derived by averaging of proper grain characteristics. Specifically, an assumption about the interdependence of levels is employed, like the commonly used Taylor and Reuss homogenization scheme [10]. The statistical models are more efficient computationally in comparison with direct and self-consistent models. Up to date, the statistical models are successfully

employed for simulation of mechanical response of large-sized parts from various materials [10,13]. Hence, the same approach is selected in the present paper. The equations of the primary constitutive model [10] are extended with auxiliary relationships on microstructure formation in WAAM processes. For robust verification, the obtained results of calculations are matched with the direct model in Section 3. The model describes the early stage of plastic deformation, where inelastic deformation is realized by dislocation slips. This study does not explore intensive plastic deformations where twinning controls the inelastic behavior of 316L SS. Instead, it assumes that existing twins stop the dislocation slips (similarly to [8]). The proposed constitutive model is assumed under isothermal conditions because the influence of variations in temperature and strain rate is small. However, the model can easily accomplish these effects by including dissipative terms. In the statistical constitutive model, the crystallites are γ-austenite grains with the face-centered cubic lattice. The presence of δ-ferrite in the material can be effectively accounted for through the hardening law because the amount of δ-ferrite is only a few percent [16] as confirmed by our experiments.

The deformation of a representative macro-volume of polycrystalline material (metal alloy) is described by applying the suggested two-level statistical model of crystal plasticity. The weighted Kirchoff stress tensor at the macro-level $\mathbf{K}$ and the effective elastic properties $\mathbf{\Pi}$ the macro-level are determined by averaging the appropriate values:

$$\mathbf{K} = \left\langle \boldsymbol{\varkappa}_{(i)} \right\rangle, i = 1,..., N \tag{1}$$

$$\mathbf{\Pi} = \left\langle \mathbf{\pi}_{(i)} \right\rangle, i = 1,..., N \tag{2}$$

$\boldsymbol{\varkappa}_{(i)} = \frac{\varrho}{\hat{\varrho}} \boldsymbol{\sigma}_{(i)}$ is the weighted Kirchoff stress tensor at the meso-level for the i-th crystallite, $\boldsymbol{\sigma}_{(i)}$ is the Cauchy stress tensor at the meso-level for the i-th crystallite, $\varrho\left(\hat{\varrho}\right)$ denote the material density in the reference (current) configuration, $\mathbf{\pi}_{(i)}$ is the elastic tensor of the i-th considered crystallite, the components of this crystallite were determined and appeared to be constant in the basis $\mathbf{k}_i$ of the rigid moving coordinate system rotating with spin $\boldsymbol{\omega}$, and $\mathbf{o}$ is the tensor which combines the moving coordinate system with the laboratory coordinate system [10]:

$$\boldsymbol{\omega} = \dot{\mathbf{o}} \cdot \mathbf{o}^{\mathrm{T}} = \mathbf{I} \times (\mathbf{k}_3 \mathbf{k}_1 \mathbf{k}_2 - \mathbf{k}_2 \mathbf{k}_1 \mathbf{k}_3 + \mathbf{k}_1 \mathbf{k}_2 \mathbf{k}_3) : \mathbf{l}^e \tag{3}$$

$\mathbf{l}^e = \mathbf{z} - \mathbf{z}^{in}$ is the elastic component of the transposed relative velocity gradient at the meso-level. For each crystallite $i = 1,..., N$ (the crystallite number is omitted), the elastic law in the rate relaxation form is used as a basic constitutive relation at the meso-level.

$$\boldsymbol{\varkappa}^{cr} = \mathbf{\pi} : \left(\hat{\nabla} \mathbf{v}^{\mathrm{T}} - \boldsymbol{\omega} - \mathbf{z}^{in} \right) \tag{4}$$

$\boldsymbol{\varkappa}^{cr} = d\boldsymbol{\varkappa} / dt + \boldsymbol{\varkappa} \cdot \boldsymbol{\omega} - \boldsymbol{\omega} \cdot \boldsymbol{\varkappa}$ is the corotational derivative of the tensor $\boldsymbol{\varkappa}$, $\hat{\nabla} \mathbf{v}^{\mathrm{T}} = \mathbf{l}$ is the meso-level velocity gradient ($\mathbf{v}$ is the meso-level velocity vector), and $\mathbf{z}^{in}$ is the inelastic component of the transposed relative velocity gradient at the meso-level.

The inelastic component $\mathbf{z}^{in}$ related to dislocation slips is determined as:

$$\mathbf{z}^{in} = \sum_{k=1}^{K_s} \dot{\gamma}^{(k)} \mathbf{b}_s^{(k)} \mathbf{n}_s^{(k)} \tag{5}$$

$$\dot{\gamma}_s^{(k)} = \dot{\gamma}_0 \left(\frac{\tau_s^{(k)}}{\tau_{cs}^{(k)}} \right)^{m_s} H\left(\tau_s^{(k)} - \tau_{cs}^{(k)} \right) \tag{6}$$

$$\tau_s^{(k)} = \mathbf{b}_s^{(k)} \mathbf{n}_s^{(k)} : \boldsymbol{\varkappa} \tag{7}$$

where $\dot{\gamma}_s^{(k)}$ is the shear rate acting on the k-th intragranular slip system, $\mathbf{b}_s^{(k)}, \mathbf{n}_s^{(k)}$ are the unit vectors of the slip direction and the normal to the k-th slip system, $\dot{\gamma}_0$ is the shear rate acting on the slip system when the shear stress reaches the critical shear stress, m_s is the strain rate sensitivity exponent of the material at dislocation slip and twinning, $\tau_s^{(k)}, \tau_{cs}^{(k)}$ are the shear and critical shear stress of the k-th slip system, and H is the Heaviside function. The critical shear stress evolution is determined by the known quasi-linear relationship [10]:

$$\dot{\tau}_{cs}^{(k)} = \sum_{j=1}^{N_s} h^{(kl)} \dot{\gamma}_s^{(j)} \tag{8}$$

$$h^{(kl)} = \left[q_{lat\_s} + (1 - q_{lat\_s}) \delta^{(kl)} \right] h^{(l)}, \qquad h^{(l)} = h_0 \left| 1 - \tau_{cs}^{(l)} / \tau_{sat\_s} \right|^{a_s} \tag{9}$$

where $h^{(kl)}$ is the matrix describing crystal hardening that arises because of the interactions between dislocations and forest dislocations, q_{lat_s} is the latent hardening parameter characterizing the location of slip systems relative to the initial twins formed in SLM, $\delta^{(kl)}$ is the Kronecker delta, τ_{sat_s} are the slip saturation stresses, h_0, a_s are the slip system hardening parameters, and K_s, is the number of slip and twinning systems in the crystallite under consideration. The dot above the corresponding variables shows the time derivative t, the superscript T represents the transpose operation of the value of the second rank tensor, the superscript (–1) represents the operation of determination of an inverse, and $\langle\ \rangle$ is the meso-level volume averaging operator.

The present work focuses on the early stage of plastic deformation, and therefore the hardening law is applied with sufficient accuracy to slip (8). Here, the interaction of dislocations with twins generated during deformation is ignored. In relation to initial critical shear stresses $\tau_{cs0}^{(k)}$, the developed model mostly relies on the assumptions presented in [12]. The initial critical shear stresses $\tau_{cs0}^{(k)}$ depend on the status of grain and cell boundaries, initial twin boundaries and lattice resistance. The value of $\tau_{cs0}^{(k)}$ is determined by the relations from [12], which describe the initial critical shear stresses according to the Hall-Petch relationship:

$$\tau_{cs0}^{(k)} = \tau_0 + k_y \left(d \right)^{-0.5} \tag{10}$$

where τ_0 is the lattice resistance of the k-th slip system, d is the mean free path length of dislocations, and k_y is the Hall-Petch coefficient; options for determining d and k_y depending on the morphology of the considered grain are described below.

The presence of twins' boundaries is one of the main factors promoting an increase in critical stresses for the initiation of slipping and twinning mechanisms and consequently the yield stress. According to the obtained data, the twins of the SLM-produced samples have a lamellar structure [18] and are characterized by a sharp change in the crystal lattice orientation [14]. The orientation of the crystallographic coordinate system of the twinning part of the crystal of the system k with respect to the crystallographic coordinate system of the original crystal is determined by the orthogonal vector $\mathbf{r}_{tw}^{(k)}$ [14]:

$$\mathbf{r}_{tw}^{(k)} = 2\mathbf{n}_{tw}^{(k)} \mathbf{n}_{tw}^{(k)} - \mathbf{I} \tag{11}$$

where $\mathbf{I}$ is the unit tensor, and $\mathbf{b}_{tw}^{(k)}, \mathbf{n}_{tw}^{(k)}$ are the unit vectors of the twin shear direction and the normal to the habitus plane k. Just similar to [12], we assume that the slip and twinning systems in which the Burgers vector (perfect dislocation for slip systems, and twinning dislocation for twin systems) lies in the habitus plane of the initial annealing twins (Fig. 4) are soft or the slip plane is parallel to the habitus plane of these twins. The rest of the slip systems are considered being rigid. For instance, for the twins with a habitus plane (111), both slip $\left[0\bar{1}1\right](111)$, $\left[0\bar{1}1\right](\bar{1}11)$, $\left[\bar{1}10\right](111)$, $\left[\bar{1}10\right](11\bar{1})$, $\left[\bar{1}01\right](111)$, $\left[\bar{1}01\right](1\bar{1}1)$ and twinning systems $\left[1\bar{2}1\right](111)$, $\left[11\bar{2}\right](111)$, $\left[\bar{2}11\right](111)$ are soft.

Another reason that the movement of dislocations slows down and the critical shear stresses increase is grain and cell boundaries. It is assumed that the cell boundaries are partially permeable for dislocations and the grain boundaries are impermeable. Thus, for a soft slip, a physically justified choice of the value of the mean free path parameter d is the value of the grain size d_{gr}. The parameter k_y describes the effect of cell boundaries. For a rigid slip, the free path length of perfect dislocations is determined by the characteristic distance d_{tw} between twins. As we consider only the early stage of plastic deformation, at which the material structure changes slightly, the value of d_{tw} is assumed to be constant. Because of a significant difference in the characteristic dimensions d_{gr} and d_{tw}, the Hall-Petch coefficients k_y are also found to be different for soft and rigid systems, and they are denoted as k_y^{soft}, k_y^{hard}, respectively.

The macro- and meso-scale levels are linked under the extended Taylor's hypothesis of strain rate homogeneity (top-down transition of the kinematic influences): $\mathbf{1} = \hat{\nabla}\mathbf{v}^{\mathrm{T}} = \hat{\nabla}\mathbf{V}^{\mathrm{T}} = \mathbf{L}$. In order to implement uniaxial tension in the framework of this model, a symmetric velocity gradient with a prescribed component L_{33}, as well as other components, are calculated to fulfill the condition $\dot{\Sigma}_{ij} = 0,\ (ij) \neq 33$, where $\mathbf{\Sigma} = \langle \boldsymbol{\sigma} \rangle$ is the Cauchy stress tensor [10].

The developed constitutive model was identified using the microstructural data summarized in Section 1 and the deformation curve No. 1 (Fig. 2) at the stage of elastic deformation and at the early stage of plastic deformation.

The identification procedure involves two steps:

1. First, the elastic moduli п_{1111}, п_{1122}, п_{1212} are determined from the segment of the experimental uniaxial tension curve in the strain range between 0.0 and 0.2 %.

2. Second, the inelastic parameters of the model $\dot{\gamma}_0$, m_s, τ_0, k_y^{soft}, k_y^{hard}, h_0, τ_{sat_s}, q_{lat_s}, a_s are identified from the experimental curve in the strain range between 0.2 and 5 %. With the same orientation, the conditions are selected to activate soft slip systems sooner than rigid ones.

When identifying parameters, the question is how to minimize the discrepancy (squared deviation) between experimental results and calculated values. For the strain ranges given above, the Nelder-Mead method has been used. The identification procedure includes (i) expert assessments for the ranges of variable parameters based on the literature data and (ii) the penalty function method to reduce a problem with constraints to a problem without constraints. Because the model has various parameters that vary significantly, the original domain was scaled to an N-dimensional cube in a dimensionless space. In this space, the model's sensitivity to variations in specific parameters was considered. Next, equally weighted coefficients were assumed to identify elastic properties. The model's high sensitivity to initial and saturation stress was considered when identifying plastic properties. Different starting points were tested in the model's parameter space to create an initial simplex (Nelder-Mead). Thus, the parameters selected had the lowest discrepancy in the objective function.

The experimental data and identified model parameters of 316L are summarized in Tab. 2 below with direct references to the source. Notably, the parameters for high-porosity materials provide a decrease in the elastic moduli that should be interpreted as the effective properties of a porous medium. The parameters of grain size d_{gr}, approximated by ellipsoids, and the residual stresses $\boldsymbol{\varkappa}_0$ were determined by the statistical distribution laws. Both the characteristics of grain structure and residual stresses are the internal model variables.

Then, this approach applies to determine the grain size distribution law d_{gr}. Based on the results of the experiments (Fig. 3), the grain size distribution and lengths measured on thin sections in three mutually orthogonal directions (r, w and h correspondingly) are log-normal. Next, it is assumed that a grain has the form of an ellipsoid with semi-axes $r/2$, $w/2$, $h/2$. After that, a sample set of these ellipsoids is generated. The spheres of equal volume with diameter d_{gr} are placed in correspondence to these ellipsoids with the average value M(d_{gr}) and standard deviation δ(d_{gr}) given in Tab. 2. The statistics of r and w is close, which is consistent with the internal symmetry of the sample built in the vertical direction.

Based on the experimental data presented in Fig. 4, the average distance between twins d_{tw} in the material was determined.

The distribution law for the residual stress tensor $\boldsymbol{\varkappa}_0$ is obtained from the experimental data given with the following assumptions:

1) The main directions of the residual stress tensor $\boldsymbol{\varkappa}_0$ coincide with the axes of SLM processing (axis 3 is the building direction) and with the axes of the laboratory coordinate system.

2) The basic values of $\varkappa_1, \varkappa_2$ of $\boldsymbol{\varkappa}_0$ coincide and the third value of $\varkappa_3$ in the build direction is equal to zero. This occurs because of the conditions of sample manufacturing through the vertical deposition. Crystallization of local areas in the radial direction leads to hardening in the radial direction owing to an already hardened frame in this direction. Thus, the hardness in the vertical direction is significantly smaller.

3) The experimentally obtained values of residual stresses $\varkappa_1 + \varkappa_2 = 190$ MPa are maximal, i.e., $\varkappa_{1\max} = \varkappa_{2\max} = 95$ MPa.

4) The distribution for the values of $\varkappa_1, \varkappa_2$ is assumed to be normal [25] with the mathematical expectation $\mathrm{M}(\varkappa_1) = \mathrm{M}(\varkappa_2) = 0$ MPa and standard deviation $\delta(\varkappa_1) = \delta(\varkappa_2) = \varkappa_{1\max} / 3$.

The calculated values of the normal distribution law parameters for the values of $\varkappa_1, \varkappa_2$ residual stress are given in Tab. 2.

To model original crystallographic textures, the samples of orientations were generated under special distribution laws. The orientations occurred randomly by applying the method of inverse transformation of the isotropic model functions of texture components, which provided the local density approximation. Based on the experimental data set in an inverse pole figure [19], the type and proportions of texture components were identified from the acceptable sample of orientations using the cluster analysis technique described in detail in [26] (Fig. 5). The scattering angles determining the localization of texture components were estimated by the maximum likelihood method.

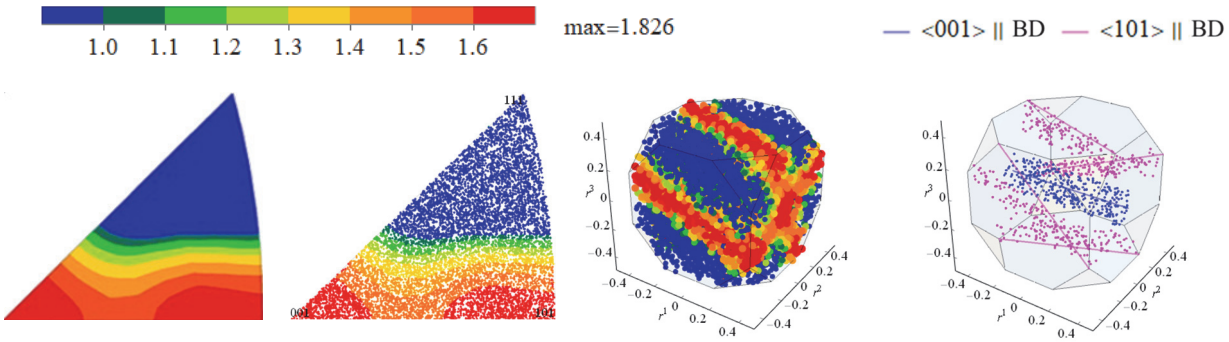

(a) (b) (c) (d)

Figure 5: Crystalline orientation samples generated with inverse pole figure. (a) Attached image of inverse pole figure. (b) Acceptable weighted sample of randomly distributed orientations. (c) Projection of the corresponding sample onto the fundamental set in the Rodrigo space. (d) Analogous projection of the generated equally weighted sample.

Parameter	Value	Source
Π_{1111}	$205 \cdot 10^3$ MPa	Identification procedure (from the elastic segment)
Π_{1122}	$133 \cdot 10^3$ MPa	Identification procedure (from the elastic segment)
Π_{1212}	$99 \cdot 10^3$ MPa	Identification procedure (from the elastic segment)
k_y^{hard}	70 MPa m$^{1/2}$	Identification procedure (from the plastic segment)
k_y^{soft}	410 MPa m$^{1/2}$	Identification procedure (from the plastic segment)
τ_0	70 MPa	Identification procedure (from the plastic segment)
h_0	1350 MPa	Identification procedure (from the plastic segment)
$\tau_{sat\_s} / \tau_{cs0}$	1,799	Identification procedure (from the plastic segment)
a_s	2,25	Identification procedure (from the plastic segment)
q_{lat_s}	1,4	Identification procedure (from the plastic segment)
d_{tw}	0,345 μm	Experimental data
$\dot{\gamma}_0$	0,00001 s^{-1}	Identification procedure (from the plastic segment)
m_s	60	Identification procedure (from the plastic segment)
$\mathrm{M}(d_{gr})$	120 μm	Experimental data
$\delta(d_{gr})$	15 μm	Experimental data
$\mathrm{M}(\varkappa_1) = \mathrm{M}(\varkappa_2)$	0 MPa	Experimental data
$\delta(\varkappa_1) = \delta(\varkappa_2)$	32 MPa	Experimental data
b_p	0,147 nm	[27]
γ_{SFE}	64 mJ/m^2	[28]
G	$44 \cdot 10^3$ MPa	Experimental data

Amount of TC <100>	0,35	Cluster analysis apparatus (technique) [26]
Scattering angle for TC <100>	9°	Cluster analysis apparatus [26]
Amount of TC <110>	0,55	Cluster analysis apparatus [26]
Scattering angle for TC<110>	9,5°	Cluster analysis apparatus [26]
Fraction associated with uniform distribution of orientations $(1-\alpha_1-\alpha_2)$	0,1	Cluster analysis apparatus [26]

Table 2: Experimental data and constitutive model parameters for 316L SS samples with parameter identification techniques and literature sources. The identification procedure is defined as the determination of the constitutive model parameters during the solution of the optimization problem planned above. The experimental data are related to the results obtained in the present study.

In summary, the developed statistical model accounts for both elastic and inelastic deformations in SLM-manufactured AISI 316L SS samples. Plasticity is introduced in the model through the mechanism of edge dislocation glide. The effect of hardening is described through the interaction of moving dislocations with grain boundaries, twins and forest dislocations. The initial two-level model was strictly verified by the authors on various polycrystal materials [10,29]. The modification suggested in the present paper is based on the well-established Hall-Petch law [12], splitting of slip planes on soft and hard because of the presence of twins in microstructure [14] and accounting for residual stresses [25]. This versatility of multi-level models toward different physical mechanisms of deformation in polycrystal materials yields adequate results, which fairly correlate with experimental data (see Section 3).

RESULTS AND DISCUSSION

This section presents the results and discussion of modeling using the described constitutive model for the uniaxial tension of the SLM-manufactured AISI 316L SS samples.

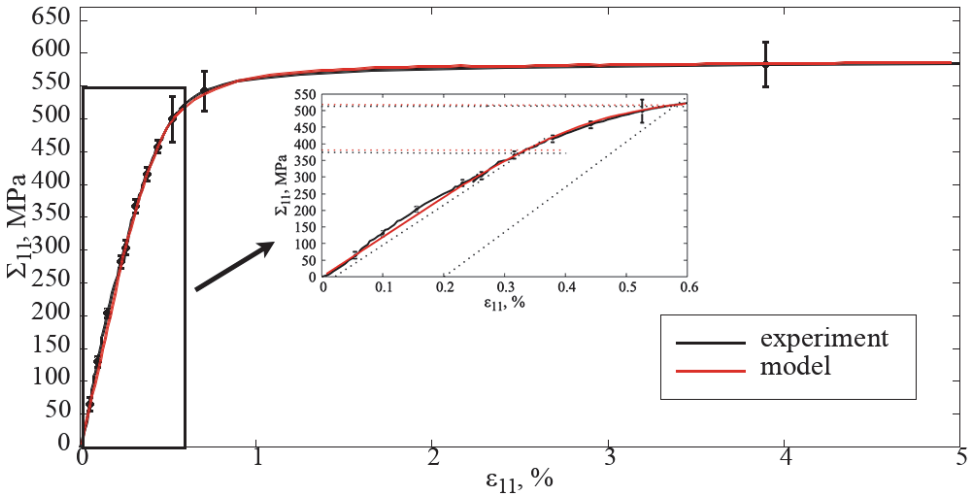

Figure 6: Experimental and calculated stress-strain diagrams in the elastic-plastic region of deformation up to 5% accumulated strain for the uniaxially loaded 316L SS samples.

Model validation

Fig. 6 illustrates the comparison between the experimental and calculated data in the regions of elasticity and plasticity up to 5% of the accumulated strain. The maximum relative deviation of the stress-strain curves in the elastic deformation region is below 4%. Observed oscillations in the experimental results are caused by the setup error. The calculated Young's modulus

is equal to $120 \cdot 10^3$ MPa. The maximum relative deviation of the stress-strain curves in the plastic deformation region (above 0,4% of accumulated strains) does not exceed 0,6%.

Tab. 3 contains the values of the yield stress σ_x at different tolerances 0,2% and 0,02% of the residual deformation. Both the experimental and calculated stresses are provided. The theoretical yield stresses are evaluated from the stress-strain diagram as follows. The lines parallel to the elastic segment and passing through the selected tolerance level x are drawn. Then, the points of intersection of these lines with the deformation curve correspond to the proper tolerance (see the inset in Fig. 6).

Identification technique	Yield stress magnitude $\sigma_{0.02}$ (MPa)	Yield stress magnitude $\sigma_{0.2}$ (MPa)
Constitutive model	381	519
Experiment	374	516

Table 3: Comparison of the yield stresses determined experimentally and calculated using the developed constitutive model.

Comparison of the statistical and direct constitutive models

The accuracy of the statistical constitutive model was tested by comparing to a direct model, which determines non-homogeneous stress-strain fields at the meso-level in the closed-packed interconnected grain structure. A more detailed description of the direct model structure is provided in [11], where the meso-level relationships of the developed constitutive model (Section 2) are used as the meso-level constitutive relationships. The application of a direct constitutive model for analysis of technological processes is hampered by its high resource intensity. Therefore, the present work is concentrated on the formulation and study of the statistical constitutive model as a much faster approach [10].

For the direct constitutive model, the original grain structure was generated based on the obtained experimental data using the open-source software Neper [30]. The considered sample contained 2000 grains. Each grain was divided into 800 elements, and the number of finite elements approached 1.6 million. The displacement velocities, which correspond to the longitudinal strain rate 10^{-3} s^{-1}, were set at the ends of the sample perpendicularly to its axis. For other facets, the trivial static boundary conditions (load-free boundaries) were specified. In contrast with the statistical constitutive model, the velocity gradients for each integration point were received from the solution to the boundary-value problem. Thus, the non-uniformity of the stress-strain state of grains was properly included.

In order to find the stress-strain fields, the original finite-element solver is used. Fig. 7 shows the stress intensity fields, collected in the numerical simulation of the 316L SS samples experiment subjected to uniaxial tension.

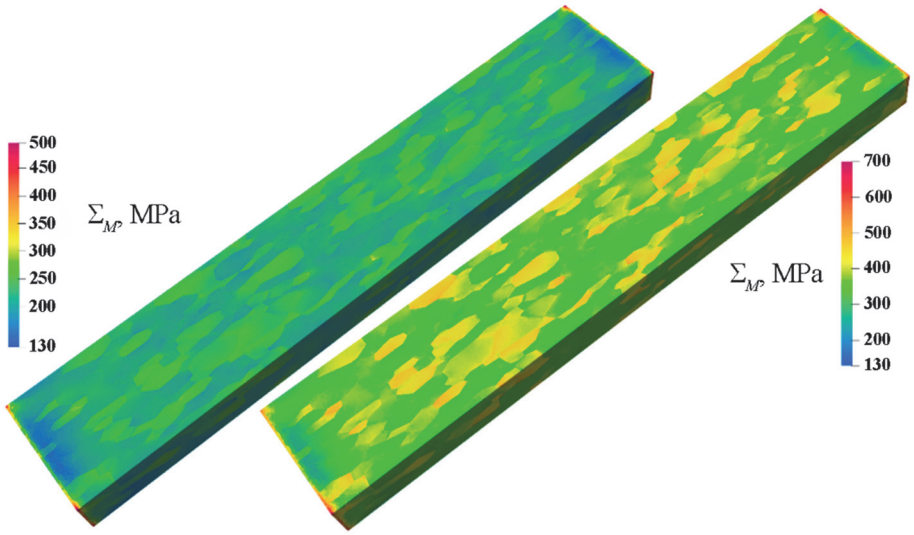

Figure 7: Stress intensity fields simulated in the uniaxial tensile test of the 316L SS samples at the 0.02% (left) and 0.2% (right) accumulated plastic strains. The mean grain size is 120 μm.

In align with the results depicted in Fig. 7, a spatial variation of stress intensity is observed at the initial (at deformations of 0.02% and 0.2%) stage of plastic deformation. The inhomogeneity is connected to the deformation process of specific grains. It becomes more significant as the inelastic deformation increases. Fig. 8 presents the stress intensity fields collected

in the numerical experiment on uniaxial tension at the relative elongations of 1%, 2% and 3%. Here, the difference in stress intensity of neighboring grains is induced by crystallographic texture. Some grains are unfavorably oriented to provide the soft slip system for dislocation gliding. Then two factors are considered as governing with (i) orientation of the grain's crystal lattice regarding the mechanical load; (ii) dominant orientation of twins in the grain. Smaller grains additionally exhibit a higher stress level in agreement with the Hall-Petch law because of a shorter free path of dislocations. Inelastic deformation begins in these systems later and develops along the hard slip systems, and thus the stress level in grains is higher. Fig. 9 gives the calculated σ–ε diagrams that match the direct and statistical models to the experimental curve in the elastic-plastic region up to 5% of accumulated strains.

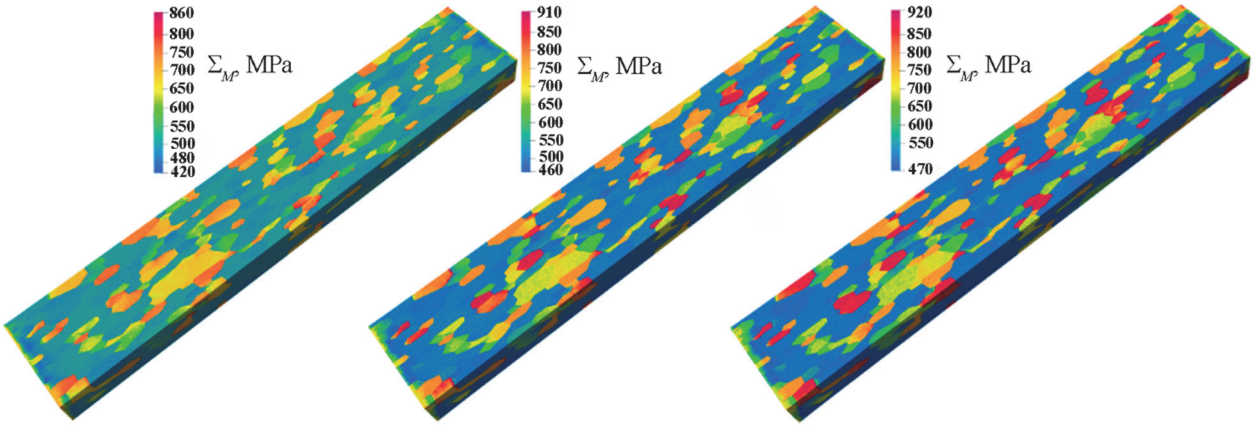

Figure 8: Stress intensity fields derived from uniaxial tensile tests conducted with 316L stainless steel samples. The figures from left to right correspond to the relative elongations of 1%, 2%, and 3%. The mean grain size is 120 μm.

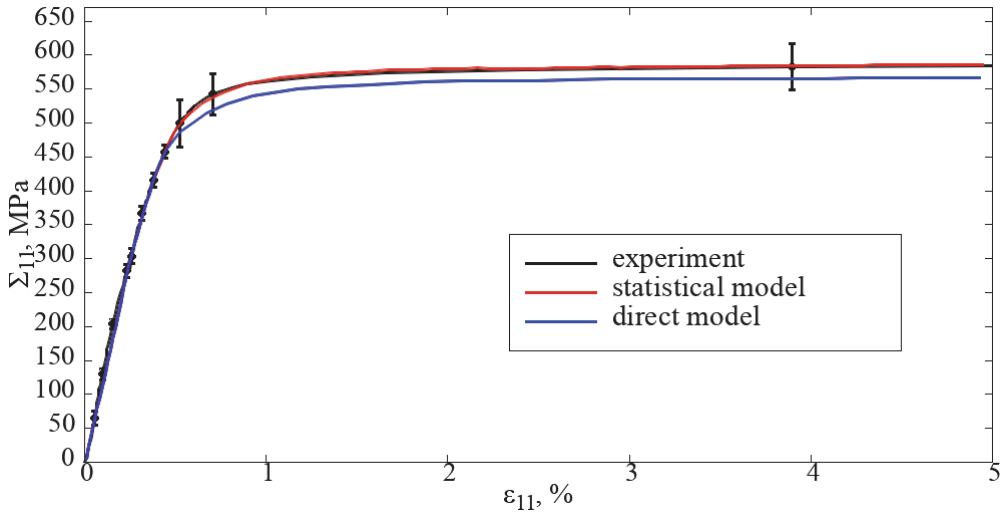

Figure 9: Averaged stress-strain curves predicted by the direct and statistical models for the uniaxial tension of the 316L SS sample. The mean grain size is 120 μm. The curves are calculated in the elastic-plastic domain up to 5% of the accumulated strain.

The difference between the direct and statistical models is explained as follows. The statistical constitutive model is based on the extended Taylor's hypothesis of strain rate homogeneity, i.e. the kinetic effects applied to each grain are the prescribed ones. These effects can be termed "rigid" effects. However, the elastic properties of cubic crystallites and a polycrystal as a whole are highly isotropic. Therefore, the results for the elastic deformation region remain practically unchanged up to the total deformations of the order of 0.2%.

The crystallographic texture induces plastic anisotropy because of slip activation preferentially in favorably oriented grains. This is the reason the curves diverge slightly (by only 3%) near plastic deformation. In the statistical model, the deformation of all grains develops in the same way, and this yields the upper stress estimates. In the direct model, the inelastic deformation of grains in the boundary-value problem is redistributed in favor of the grains oriented toward the slip of soft systems. Therefore, the plastic deformation of the grains oriented toward the slip of rigid systems begins later (Fig. 8). Thus, the deformation curve plotted based on the results of the direct model lies somewhat below the corresponding loading curve

of the statistical model (Fig. 9). With the parameter identification for the direct model, then its correspondence to the experimental data will be closer. The identified parameters of the crystallite elastic moduli and saturation stress in the law of mesoscale hardening will be greater compared to those used here. For such parameters of the statistical model, the resulting deformation curve will lie somewhat higher than the experimental curve. Thus, the results of direct modeling yield a quantitative confirmation of the efficacy of the developed constitutive model. Let us now analyze the results got with the statistical constitutive model.

Sensitivity of the statistical model to parameter variations

The results showing how the constitutive model parameters affect the stress-strain state of the SLM samples are given below. The yield stress magnitudes $\sigma_{0.02}$, $\sigma_{0.2}$ calculated at different maximum values of residual stresses are presented in Tab. 4. It is seen that the residual stresses introduced into the constitutive model by the technique mentioned above have only a slight effect on the yield stresses $\sigma_{0.02}$, $\sigma_{0.2}$. The yield stress values retrieved in the statistical constitutive model at different mean grain sizes are presented in Tab. 5 and shown in Fig. 10.

Level of maximum residual stresses, MPa	Yield stress magnitude $\sigma_{0.02}$, MPa	Yield stress magnitude $\sigma_{0.2}$, MPa
0	381	530
23	381	530
45	381	530
95	381	530
190	373	530
270	368	528
380	365	527

Table 4: Dependence of the yield stresses $\sigma_{0.02}$, $\sigma_{0.2}$ on the level of maximum residual stresses.

Mean grain size, μm	Yield stress magnitude $\sigma_{0.02}$, MPa	Yield stress magnitude $\sigma_{0.2}$, MPa
110	385	534
120	381	530
130	378	527

Table 5: Dependence of the yield stresses $\sigma_{0.02}$, $\sigma_{0.2}$ on mean grain sizes.

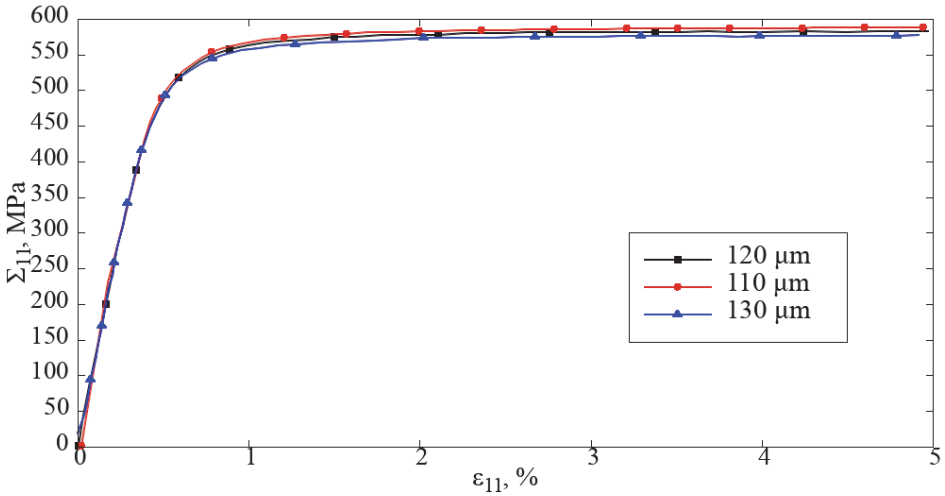

Figure 10: Curves of the σ–ε uniaxial loading diagram plotted for the representative volume of the 316L SS samples using the identified constitutive model. The different curves correspond to variable mean grain sizes.

The results from Tab. 5 and Fig. 10 indicate an inverse dependence between the yield stresses $\sigma_{0.02}$, $\sigma_{0.2}$ and the square root of the mean grain size. The smaller the grain, the higher the flow strength. This is consistent with the Hall-Petch law. The yield stress magnitudes $\sigma_{0.02}$ and $\sigma_{0.2}$ alter by 1,8% and 1.3% correspondingly if and the mean grain size varies from 110 to 130 μm. It means that the relative variation of the yield stress is much lower than the imposed variation of the residual stress. This relationship corresponds to the prescribed Hall-Petch relationship at the initial critical shear stresses of slip and twinning systems of the constitutive model.

One way to check the validity and accuracy of the developed mathematical model is the stability assessment regarding its parameter perturbations as suggested in [15,29]. Let us outline the algorithm for numerical analysis of the model stability and apply it to the developed two-level constitutive model of the 316L SS sample deformation. The first step involves identifying the primary solution without perturbations for a material response, i.e. variation in the stress-strain state of steel under the action of prescribed loads. Then, the stability of the model is studied regarding this solution. The basic solution suggests variations in the stress-strain curve of the 316L SS samples subjected to uniaxial tension. In the second step, the parameter-related perturbations are set and the model response is studied. More information about specifying model perturbations is given in [15].

Consider the stability of the constitutive model to perturbations in the parameters τ_0 and d_{tw} at the initial stage of deformation. In the general case, the value of the perturbed parameter A^* is equal to $A^*(0)=A(0)(1+\alpha)$, where A is the parameter value selected with the primary solution. Here, α is the random value, uniformly distributed in the range $[-\delta,\delta]$. The perturbed parameters are chosen based on their physical context. The parameter τ_0 describes the lattice resistance to dislocation motion, meaning that this parameter considers the influence of sufficiently thin elements of the internal structure like (e,g., cell boundaries, grain dislocation density) on the hardening of the material. The parameter d_{tw} is the characteristic distance between twins after laser deposition. In addition, it contributes considerably to material hardening. Thus, the selected parameters are the governing characteristics of the internal material structure, but their identification requires complex and rather expensive experiments. Hence, it is reasonable to validate the model response to variation of these parameters. Notably, the indicated parameters enter the hardening law, which is a key meso-level equation that governs the material behavior at the macro-level.

The third step requires generating the program of experiments, which should include different primary solutions and parameter perturbations. In the present study, a separate perturbation of the above parameters at only one primary solution is considered. In the fourth step, a series of computational experiments are implemented according to the program, and the values of ranges of a relative perturbation in the parameters δ are determined. The fifth step is the validation of stability conditions presented in [29] where the relative deviation norms of the perturbed parameter are computed. For this purpose, the values of the relative deviation norms of the perturbed parameters $\Delta_A=\dfrac{\|A^*(0)-A(0)\|}{\|A(0)\|}$ and the response $\Delta_\kappa=\dfrac{\|\mathbf{K}^*(t)-\mathbf{K}(t)\|}{\|\mathbf{K}(t)\|}$ are calculated [29]. The values of the norms got for each computational experiment is conveniently represented graphically (Fig. 11).

Fig. 11 shows that as the relative norm of perturbed parameters decreases, the relative norm of the response also diminishes. It shows the stability of the model consistent with the definition given in [29]. The perturbation τ_0 has a greater effect on the response deviation. Thus, a more comprehensive work on finding τ_0 in the constitutive model is required. For the perturbation d_{tw}, there is a significant difference in the relative deviation norms of the response received at similar values of the relative deviation norms of this parameter. Two straight lines diverge in Fig. 11b. It happens because this parameter can either increase or decrease at different computational implementations of d_{tw} perturbations. If it decreases, the relative deviation norm of the response appears to be higher compared to the case when it increases by a similar value of the perturbation.

The developed statistical constitutive model naturally relates the microstructure of the SLM-produced 316L SS sample and its mechanical properties. It can serve as a basis for creating an effective digital design tool for getting functional products and structures. For instance, it permits determining laser deposition regimes to get the best performance properties of the product depending on the current state of the material structure. The model can be embedded in modern FEM-based software packages, which allow predicting the stress-strain state of the material and calculating its strength properties. Then, the products and structures adapted to operating conditions can be built.

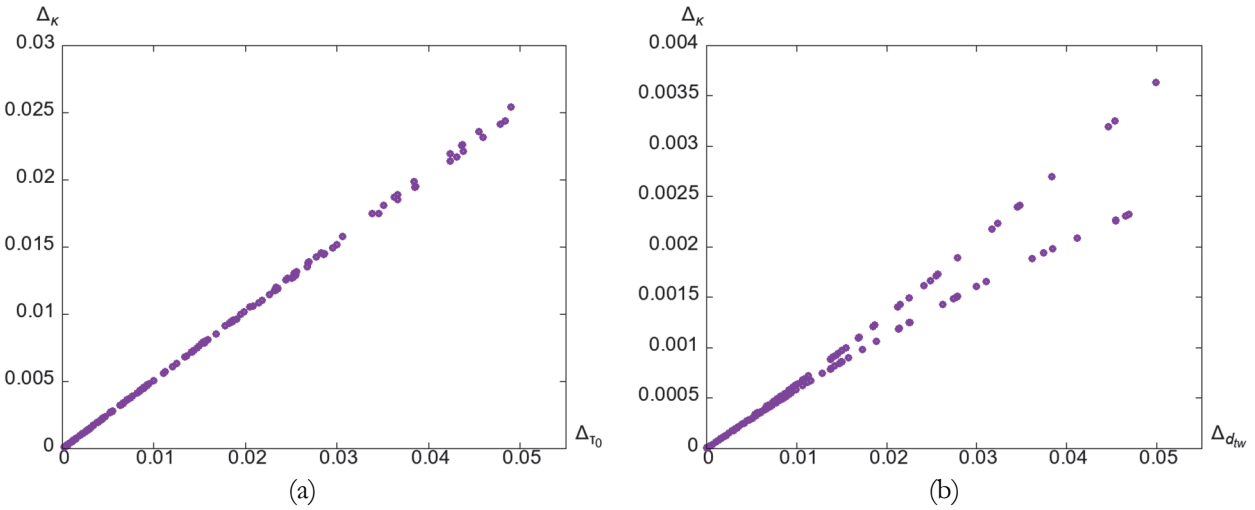

Figure 11: Sensitivity analysis at the relative ranges of parameter perturbations $\delta = 0.01$, $\delta = 0.03$, $\delta = 0.05$. (a) Δ_κ vs. Δ_{τ_0}. (b) Δ_κ vs $\Delta_{d_{tw}}$.

CONCLUSION

Own experimental results and relevant literature data have been used for the analysis of physical mechanisms in the deformation of SLM-fabricated 316L stainless-steel samples. Based on the observed microstructure, crystal texture and measured properties of distinct structural elements, a two-level constitutive model has been developed. This model accounts for elastic viscoplastic deformation, and it includes statistical averaging over a representative polycrystal set for better accuracy. Then the model is used for calculation the basic mechanical characteristics of inelastic deformation (Young's modulus and yield stresses at different tolerances) of a representative volume of the samples. The following conclusions are drawn.

(i) The revealed results are qualitatively consistent with the data of tensile experiments displayed by the elastic and plastic parts of the deformation curve within 96 percent of accuracy.

(ii) Following the performed analysis, a higher sensitivity of the constitutive model response to the mean grain size rather than to the magnitude of residual stresses is confirmed.

The stability of the developed two-level constitutive model regarding perturbations of the lattice resistance parameters and mean distance between twins is proved established. Thus, the developed statistical constitutive model for describing the behavior of the AISI 316L SS samples can serve as a basis for the development of an effective parametric model. The latter has good prospects for rapid computer simulation of various boundary–value problems of industrial relevance.

ACKNOWLEDGEMENTS

Peter V. Trusov – consultation
Kirill V. Ostapovich – texture analysis
Anton Yu. Yants – software implementation of the direct model
Nikolay V. Kostenkov – TEM investigations
Yulia O. Kuzminova – mechanical testing of samples

FUNDING

The research part related to a comprehensive analysis of the stability of the developed model to perturbations in its parameters was funded by the Ministry of Education and Science of the Russian Federation as part of the state task in the laboratory of multilevel structural and functional materials modeling, project no. FSNM-2024-0002. The part of this study devoted to SLM sample manufacturing, mechanical tests and microstructural assessment was funded within the projects EOTP-MT-097 and Ph.D. grant SPN.2024.03151.

REFERENCES

[1] Gibson, I., Rosen, D., Stucker, B., and Khorasani, M. (2021). Additive Manufacturing Technologies, Cham, Springer International Publishing, DOI: https://doi.org/10.1007/978-3-030-56127-7.

[2] Abdulhameed, O., Al-Ahmari, A., Ameen, W., and Mian, S.H. (2019). Additive manufacturing: Challenges, trends, and applications, Advances in Mechanical Engineering, 11(2). DOI: https://doi.org/10.1177/1687814018822880.

[3] Rouf, S., Malik, A., Singh, N., Raina, A., Naveed, N., Siddiqui, M.I.H., and Haq, M.I.U. (2022). Additive manufacturing technologies: Industrial and medical applications, Sustainable Operations and Computers, 3, pp. 258–274. DOI: https://doi.org/10.1016/j.susoc.2022.05.001.

[4] Chaudhary, R., Fabbri, P., Leoni, E., Mazzanti, F., Akbari, R., and Antonini, C. (2023). Additive manufacturing by digital light processing: a review, Prog Addit Manuf, 8(2), pp. 331–351. DOI: https://doi.org/10.1007/s40964-022-00336-0.

[5] Gruzd, S.A., Lomaev, S.L., Simakov, N.N., Gordeev, G.A., Bychkov, A.S., Gapeev, A.A., Cherepetskaya, E.B., Krivilyov, M.D., and Ivanov, I.A. (2022). Analysis of the Effect of Magnetic Field on Solidification of Stainless Steel in Laser Surface Processing and Additive Manufacturing, Metals, 12(9), p. 1540. DOI: https://doi.org/10.3390/met12091540.

[6] Zhou, L., Miller, J., Vezza, J., Mayster, M., Raffay, M., Justice, Q., Tamimi, Z.A., Hansotte, G., Sunkara, L.D., Bernat, J., Zhou, L., Miller, J., Vezza, J., Mayster, M., Raffay, M., Justice, Q., Tamimi, Z.A., Hansotte, G., Sunkara, L.D., and Bernat, J. (2024). Additive Manufacturing: A Comprehensive Review, Sensors, 24(9). DOI: https://doi.org/10.3390/s24092668.

[7] Gao, B., Zhao, H., Peng, L., and Sun, Z. (2023). A Review of Research Progress in Selective Laser Melting (SLM), Micromachines, 14(1), p. 57. DOI: https://doi.org/10.3390/mi14010057.

[8] Charmi, A., Falkenberg, R., Ávila, L., Mohr, G., Sommer, K., Ulbricht, A., Sprengel, M., Saliwan Neumann, R., Skrotzki, B., and Evans, A. (2021). Mechanical anisotropy of additively manufactured stainless steel 316L: An experimental and numerical study, Materials Science and Engineering: A, 799, p. 140154. DOI: https://doi.org/10.1016/j.msea.2020.140154.

[9] Zinovieva, O., Romanova, V., Zinoviev, A., Nekhorosheva, O., and Balokhonov, R. (2023). Elastic properties of additively manufactured steel produced with different scan strategies, International Journal of Mechanical Sciences, 244, p. 108089. DOI: https://doi.org/10.1016/j.ijmecsci.2022.108089.

[10] Trusov, P.V., Shveykin, A.I., Kondratyev, N.S., and Yants, A.Yu. (2021). Multilevel Models in Physical Mesomechanics of Metals and Alloys: Results and Prospects, Phys. Mesomech., 24(4), pp. 391–417. DOI: https://doi.org/10.1134/S1029959921040056.

[11] Ostapovich, K.V., Trusov, P.V., and Yants, A.Yu. (2021). Prediction of Crystallographic Texture Formation in Polycrystalline Samples under Severe Plastic Deformation Based on a Two-Level Statistical Elasto-Viscoplastic Model, Phys Mesomech, 24(3), pp. 225–236. DOI: https://doi.org/10.1134/S1029959921030012.

[12] Mayeur, J.R. and McDowell, D.L. (2007). A three-dimensional crystal plasticity model for duplex Ti–6Al–4V, International Journal of Plasticity, 23(9), pp. 1457–1485. DOI: https://doi.org/10.1016/j.ijplas.2006.11.006.

[13] Shveykin, A.I., Trusov, P.V., and Kondratev, N.S. (2021). Multiplicative Representation of the Deformation Gradient Tensor in Geometrically Nonlinear Multilevel Constitutive Models, Lobachevskii J Math, 42(8), pp. 2047–2055. DOI: https://doi.org/10.1134/S1995080221080291.

[14] Staroselsky, A.V. (1998). Crystal plasticity due to slip and twinning. Thesis, Massachusetts Institute of Technology, 1998.

[15] Shveykin, A., Trusov, P., and Romanov, K. (2024). Stability of Crystal Plasticity Constitutive Models: Observations in Numerical Studies and Analytical Justification, Metals, 14(8), p. 947. DOI: https://doi.org/10.3390/met14080947.

[16] Kurzynowski, T., Gruber, K., Stopyra, W., Kuźnicka, B., and Chlebus, E. (2018). Correlation between process parameters, microstructure and properties of 316 L stainless steel processed by selective laser melting, Materials Science and Engineering: A, 718, pp. 64–73. DOI: https://doi.org/10.1016/j.msea.2018.01.103.

[17] Marattukalam, J.J., Karlsson, D., Pacheco, V., Beran, P., Wiklund, U., Jansson, U., Hjörvarsson, B., and Sahlberg, M. (2020). The effect of laser scanning strategies on texture, mechanical properties, and site-specific grain orientation in selective laser melted 316L SS, Materials & Design, 193, p. 108852. DOI: https://doi.org/10.1016/j.matdes.2020.108852.

[18] Sun, Z., Tan, X., Tor, S.B., and Chua, C.K. (2018). Simultaneously enhanced strength and ductility for 3D-printed stainless steel 316L by selective laser melting, NPG Asia Materials, 10(4), pp. 127–136. DOI: https://doi.org/10.1038/s41427-018-0018-5.

[19] Kumar, D., Shankar, G., Prashanth, K.G., and Suwas, S. (2021). Texture dependent strain hardening in additively manufactured stainless steel 316L, Materials Science and Engineering: A, 820, p. 141483. DOI: https://doi.org/10.1016/j.msea.2021.141483.

[20] Sinha, S., Szpunar, J.A., Kiran Kumar, N.A.P., and Gurao, N.P. (2015). Tensile deformation of 316L austenitic stainless steel using in-situ electron backscatter diffraction and crystal plasticity simulations, Materials Science and Engineering: A, 637, pp. 48–55. DOI: https://doi.org/10.1016/j.msea.2015.04.005.

[21] Qiu, C., Kindi, M.A., Aladawi, A.S., and Hatmi, I.A. (2018). A comprehensive study on microstructure and tensile behaviour of a selectively laser melted stainless steel, Sci. Rep., 8(1), p. 7785. DOI: https://doi.org/10.1038/s41598-018-26136-7.

[22] Demir, E., Martinez-Pechero, A., Hardie, C., and Tarleton, E. (2025). OXFORD-UMAT: An efficient and versatile crystal plasticity framework, International Journal of Solids and Structures, 307, p. 113110. DOI: https://doi.org/10.1016/j.ijsolstr.2024.113110.

[23] Joo, M., Wi, M.-S., Yoon, S.-Y., Lee, S.-Y., Barlat, F., Tomé, C.N., Jeon, B., and Jeong, Y. (2023). A crystal plasticity finite element analysis on the effect of prestrain on springback, International Journal of Mechanical Sciences, 237, p. 107796. DOI: https://doi.org/10.1016/j.ijmecsci.2022.107796.

[24] Aria, A.I., Holmedal, B., Mánik, T., Marthinsen, K., Aria, A.I., Holmedal, B., Mánik, T., and Marthinsen, K. (2024). A Full-Field Crystal Plasticity Study on the Bauschinger Effect Caused by Non-Shearable Particles and Voids in Aluminium Single Crystals, Metals, 14(4). DOI: https://doi.org/10.3390/met14040424.

[25] Salvati, E. and Korsunsky, A.M. (2017). An analysis of macro- and micro-scale residual stresses of Type I, II and III using FIB-DIC micro-ring-core milling and crystal plasticity FE modelling, International Journal of Plasticity, 98, pp. 123–138. DOI: https://doi.org/10.1016/j.ijplas.2017.07.004.

[26] Ostapovich, K.V. and Trusov, P.V. (2021). Reduced Statistical Representation of Crystallographic Textures Based on Symmetry-Invariant Clustering of Lattice Orientations, Crystals, 11(4), p. 336. DOI: https://doi.org/10.3390/cryst11040336.

[27] Lu, X., Zhao, J., Wang, Z., Gan, B., Zhao, J., Kang, G., and Zhang, X. (2020). Crystal plasticity finite element analysis of gradient nanostructured TWIP steel, International Journal of Plasticity, 130, p. 102703. DOI: https://doi.org/10.1016/j.ijplas.2020.102703.

[28] Hajian, M., Abdollah-zadeh, A., Rezaei-Nejad, S.S., Assadi, H., Hadavi, S.M.M., Chung, K., and Shokouhimehr, M. (2015). Microstructure and mechanical properties of friction stir processed AISI 316L stainless steel, Materials & Design, 67, pp. 82–94. DOI: https://doi.org/10.1016/j.matdes.2014.10.082.

[29] Shveykin, A.I., Trusov, P.V., and Romanov, K.A. (2021). An approach to numerical estimating the stability of multilevel constitutive models, Computational Continuum Mechanics, 14(1), pp. 61–76. DOI: https://doi.org/10.7242/1999-6691/2021.14.1.6.

[30] Quey, R. and Renversade, L. (2018). Optimal polyhedral description of 3D polycrystals: Method and application to statistical and synchrotron X-ray diffraction data, Computer Methods in Applied Mechanics and Engineering, 330, pp. 308–333. DOI: https://doi.org/10.1016/j.cma.2017.10.029.